Supplementary Information to: "Multi-isotopic and trace element evidence against different formation pathways for oyster microstructures"

Niels J. de Winter[1,2], Linda K. Dämmer[3,4], Michaela Falkenroth[3,4,5], Gert-Jan Reichart[1,3], Simone Moretti[6], Alfredo Martinez-García[6], Nils Höche[7], Bernd R. Schöne[7], Katerina Rodiouchkina[8], Steven Goderis[2], Frank Vanhaecke[8], Sonja M. van Leeuwen[9], Martin Ziegler[1]*

[1]Dept. of Earth Sciences, Utrecht University, Utrecht, the Netherlands

[2]AMGC research group, Vrije Universiteit Brussel, Brussels, Belgium

[3]Ocean Systems Department, Royal Netherlands Institute for Sea Research and Utrecht University, Texel, the Netherlands

[4]Environmental Geology, Department of Geology, Institute of Geosciences, University of Bonn, Bonn, Germany

[5]Neotectonics and Natural Hazards Research Group, Rheinisch-Westfälische Technische Hochschule Aachen, Aachen, Germany

[6]Max Planck Institute for Chemistry, Otto Hahn Institute, Mainz, Germany

[7]Institute of Geosciences, University of Mainz, Mainz, Germany

[8] Atomic and Mass Spectrometry - A&MS research group, Department of Chemistry, Ghent University, Ghent, Belgium

[9]Coastal Systems Department, Royal Netherlands Institute for Sea Research, Texel, the Netherlands

Introduction

This document details supplementary methods and results belonging to the manuscript titled "*Multi-isotopic and trace element evidence against different formation pathways for oyster microstructures*" submitted to Geochimica et Cosmochimica Acta and serves to provide additional information about the study not given in the main manuscript. In addition, the list below serves as a guideline for the reader to find the unprocessed data belonging to this manuscript in the online appendix. All supplementary data is provided in the open-source online repository Zenodo and can be accessed through the following link: http://www.doi.org/10.5281/zenodo.3904236.

Supplementary data – table of contents

S1	Full quality versions of all microscopic images (both visible light and scanning electron microscopy) and composites used to observe and describe the microstructures of *C. gigas* and, in particular, their transitions. A selection of these were used to produce Fig. 3 in the main text.
S2	Full quality color scans of hinge regions of all specimens used in this study including lines indicating the positions of XRF measurements (for those specimens on which these were done). Some of these images were used to create **Fig. 2** in the main text.
S3	Compilation of raw XRF results, processed and calibrated trace element concentrations, calculations of distribution coefficients, age model results and alignments of environmental data for all Brittany specimens (**O1-8**) on which XRF measurements were done.
S4	Compilation of raw XRF results, processed and calibrated trace element concentrations, calculations of distribution coefficients, age model results and alignments of environmental data for all Texel specimens (**H1**, **H4**, **M3-6**) on which XRF measurements were done.
S5	Compilation of Mg/Ca, $\delta^{18}O_c$ and $\delta^{13}C_c$ data from profiles through shells **M1** and **M2** as well as temperature Mg/Ca-regressions for all specimens used to test the Mg/Ca-temperature relationship.
S6	Matlab script used to model shell growth from Mg/Ca profiles adapted from Judd et al. (2018).
S7	Compilation of age model results for all individual shells including figures against depth and age of the shell showing the fit between the modelled and measured Mg/Ca profiles. **Fig. 6** in the main text is based on this data.
S8	Compilation of hourly environmental data (sea surface temperature and salinity) from the Texel localities against which shell data was compared. Data from the NIOZ jetty for the period from 2001 up to and including 2018 was supplied by Eric Wagemaakers and Sonja van Leeuwen (pers. comm.)
S9	Compilation of daily environmental data (sea surface temperature and salinity) from the Brittany locality against which shell data was compared. Data for this locality were obtained from the Institut Français de Recherche pour l'Exploitation de la Mer (IFREMER, Issy-les-Moulineaux, France; http://www.ifremer.fr/co-en/, last access 18/05/2020
S10	Summary of all data gathered within this study with tabs for each isotope system or parameter measured in the oyster shells
S11	Data appendix listing all individual clumped isotope measurements used in this study and their raw values. This file includes data on the independent IAEA-C2 and ETH standards of which repeated measurements were done over the entire measurement periods to assess machine stability and the external standard deviation reported for clumped isotope measurements.
S12	Results of sinusoidal modelling on microstructure presence, growth rate and elemental distribution coefficients to test seasonal variability in these parameters.
S13	Calculations of the temperature bias that could occur due to the non-linear temperature conversion when combining clumped isotope measurements from a seasonal archive such as a bivalve shell. Two scenarios are considered: a 50/50 combination of summer and winter temperatures and a combination of 12 equal samples from the monthly temperature means.
S14	Script used to calculate Kernel-smoothed normal distribution plots of Δ_{47} measurements in the chalky and foliated microstructures (see **Fig. S5**).

Supplementary methods

X-ray fluorescence analysis

Trace element compositions of chalky and foliated calcite in specimens **H1**, **H4**, **M3-6** and **O1-8** were analyzed by means of X-ray Fluorescence (XRF) profiles in the direction of growth through (1) both microstructures and (2) solely through the foliated microstructure (see **Fig. 4** in main text, **S2** for sampling localities and **S3-4** for raw data). XRF analyses were carried out using a Bruker® M4 Tornado lab based energy dispersive micro-XRF scanner, the description of which (summarized below) is taken from de Winter and Claeys (2016). The µXRF technique combines the advantages of an automated microscope-guided high precision (±1 µm) movable stage system with the spectral resolution of a high-energy X-ray source to allow fast, non-destructive and high-resolution (25 µm spot size; calibrated for Mo-kα radiation) elemental analysis. The polycapillary focusing and XYZ moving stage of the table-top µXRF device enable the formation of line scans and two-dimensional maps on the sample surface. The dimensions of the vacuum chamber of the µXRF device make it possible to measure sample surfaces of up to 200 mm x 160 mm. No sample coating is necessary, and the method is fully non-destructive allowing, for example, the measurement of rare and unique samples from museum collections. The internal morphology of the µXRF vacuum chamber is shown in **Figure S1**.

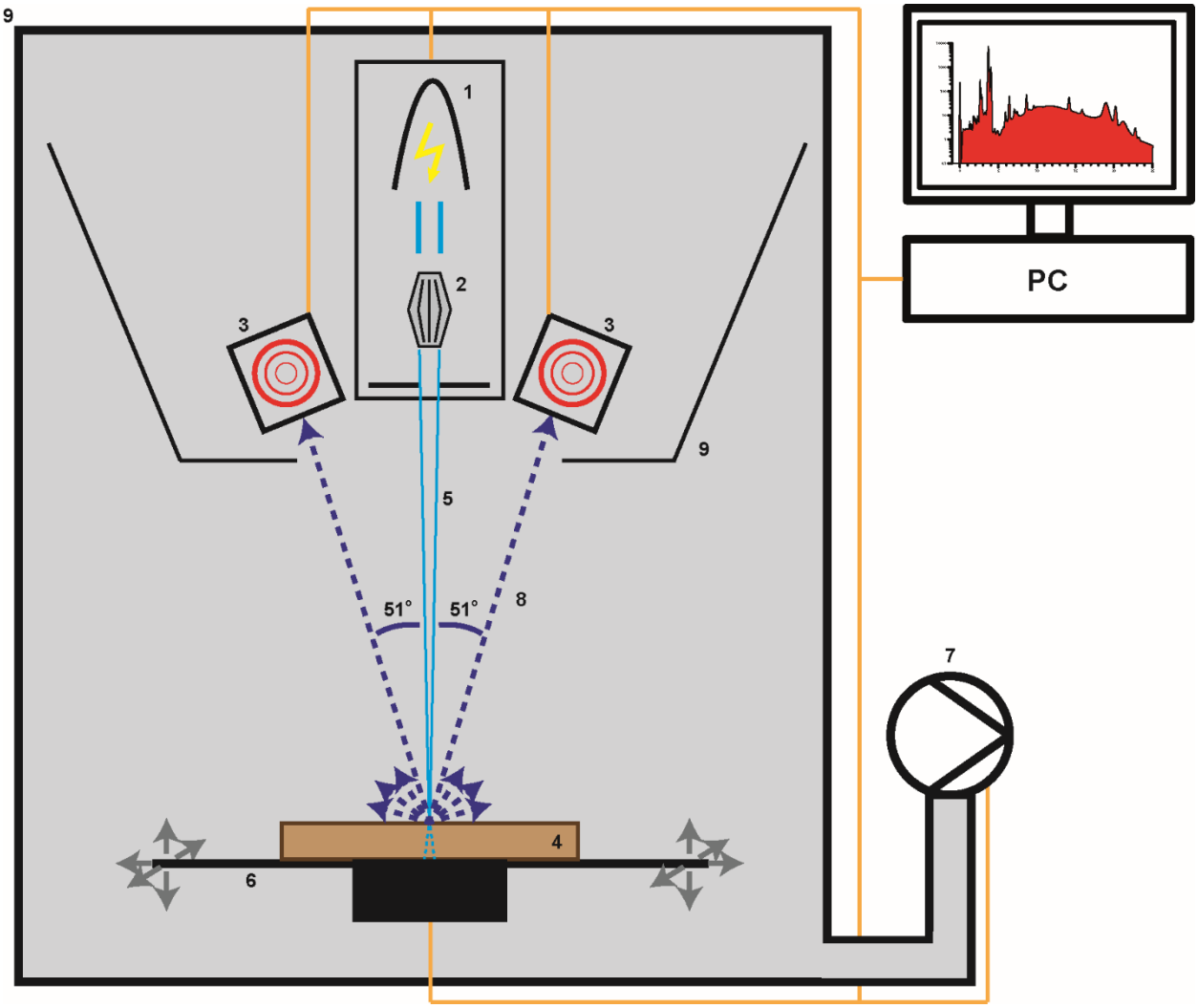

Figure S1*: Schematic overview of the Bruker M4 Tornado µXRF set-up (after de Winter and Claeys, 2016) showing the Rh X-Ray source (1), the poly-capillary optics (2), the Silicon Drift Detectors (3), the sample (4), the focused incident X-ray beam (5), the XYZ computer guided sample stage (6), the vacuum pump (7), the outgoing fluorescence hitting the detector (8) and the vacuum chamber (9). Note that the source (1) and optics (2) are positioned behind the field of view such that the incident beam (5) is aimed at an angle of 39° to the field of view. Besides their lateral angle shown in the picture, the detectors (3) are positioned to the front such that the outgoing fluorescence (8) hitting the detector forms at 51° with the field of view. As a result, the angle between incident (5) and outgoing (8) radiation is exactly 90°.*

Since sample matrix can influence the result of XRF analyses, quantification of XRF spectra requires matrix correction using a matrix-matched (carbonate) standard to produce meaningful results. In this study, we followed the recommended quantification approach by de Winter and Claeys (2016), using the BAS CRM393 limestone standard (Bureau of Analyzed sample Ltd, Middlesbrough, UK). This workflow was demonstrated to yield reproducible quantitative results for all elements of interest in this study, with spectral deconvolution errors <5% (see Table 1 in de Winter and Claeys, 2016). Note that the signal-to-noise ratio decreases for elements which fluoresce in the light end of the XRF spectrum, such as Na, which has the highest deconvolution error (4.0%). Accuracy of XRF measurements on the Bruker M4 were also tested in de Winter and Claeys (2016) by measuring a second, independent, matrix-matched carbonate standard (BAS CRM512), and was found to be <10% relative to the certified concentration for all elements of interest except for Cl, for which no certified concentration was available for this standard.

As a second step to ensure proper standardization of quantified trace element concentrations, linear calibration lines were established using a set of 7 matrix-matched standards which were treated as samples through the measurement procedure outlined above (see details in de Winter et al., 2017 and Vansteenberge et al., 2020). The slopes of these calibration curves were used to bring trace element concentrations measured on the Bruker M4 tornado into an absolute reference frame to enable comparison with other trace element measurements. The R^2 values of these calibration lines (reported most recently in Vansteenberge et al., 2020) are better than 0.99 for all elements of interest except for Cl, for which only one standard was available with a certified reference value (NIM-GBW07108; China National Analysis Center for Iron and Steel). Matrix quantification methods and calibration curves were recreated after each source calibration of the XRF Tornado to ensure drifts in source intensity did not influence the results over time. In addition, the matrix-matched BAS CRM393 carbonate standard and other reference materials were repeatedly measured on a weekly basis to check for drift of the measurement results. Finally, the high-resolution point-by-point line scanning approach (see de Winter et al., 2017) taken in this study ensured that each volume of chalky and/or foliated microstructure was sampled multiple times using independent point measurements, allowing assessment of the external precision of XRF measurements within the shell material.

Estimating seawater composition using mass balance equation

Since high-resolution (hourly or daily) *in situ* measurements of $\delta^{18}O_{sw}$ and the concentrations of trace elements in the seawater were not available, these concentrations were estimated from SSS data. Seawater $\delta^{18}O$ values were estimated using a mass balance, in which each SSS measurement was assumed to record seawater as a mix between fully marine water ($\delta^{18}O_{sw}$ ≡ 0‰VSMOW; SSS = 35 psu) mixed with a fraction (f) of freshwater with a $\delta^{18}O_{sw}$ of -7.9‰VSMOW and a SSS of 0 psu. The $\delta^{18}O_{sw}$ of freshwater was based on rainwater $\delta^{18}O$ measurements in the Netherlands (Mook, 1970) and in agreement with previously determined regional SSS-$\delta^{18}O_{sw}$ relationships (Witbaard et al., 1994; Harwood et al., 2008). The $\delta^{18}O_{sw}$ value was calculated for each SSS by solving the following mass balance equations:

$$\delta^{18}O_{sw} = \delta^{18}O_{sw,freshwater} * f + \delta^{18}O_{sw,freshwater} * (1 - f)$$

$$f = \frac{SSS_{sample} - SSS_{ocean}}{SSS_{freshwater} - SSS_{ocean}}$$

The concentration of the elements Na, Mg, S, Cl, Ca, Mn and Sr in seawater were estimated from SSS by assuming their conservative behavior at the sea surface as major constituents of marine salinity (Quinby and Turehian, 1983). This means that their concentrations are mostly driven by salinity changes and assumes their concentrations in non-marine source waters (mostly rainwater) are negligible in comparison with the concentrations in seawater. The marine concentrations ($[X]_{seawater}$ in mmol/Kg at 35 psu SSS) were obtained from Pilson (2012; for Na, Mg, Cl, S, Ca, Sr) and van Hulten et al. (2016; for Mn; summarized in **Table S1**). The same mass balance as outlined above for $\delta^{18}O_{sw}$ values allows concentrations of these elements to be calculated for each SSS data point.

Table S1: Average sea surface trace element concentrations following Pilson (2012) and van Hulten et al (2016)

Element	Concentration at 35 psu	Reference
Na	468.96 mmol/Kg	*Pilson, 2012*
Mg	52.83 mmol/Kg	*Pilson, 2012*
Cl	545.88 mmol/Kg	*Pilson, 2012*
S	28.23 mmol/Kg	*Pilson, 2012*
Ca	10.28 mmol/Kg	*Pilson, 2012*
Mn	0.004 mmol/Kg	*van Hulten et al., 2016*
Sr	0.0906 mmol/Kg	*Pilson, 2012*

Sinusoidal regression for investigating seasonality

The age model and the link between microstructure and µXRF profiles (see **2.5**) allowed us to test whether there is a seasonal component to the expression of microstructure, growth rate and the distribution coefficients of trace elements. Monthly averages of the relative contributions of foliated and chalky microstructures, growth rate along axis of maximum growth and distribution coefficients of trace elements were calculated for each specimen using the age model. The degree of seasonality in these parameters was estimated by fitting a sinusoidal function through the monthly data (see **S12**). From this fit, we extracted the significance (p-value) of the fit, the goodness of fit (adjusted R^2 value), the relative seasonal amplitude (amplitude of seasonality relative to the annual mean value) and the timing of the seasonal maximum (phase). Only parameters with a significant sinusoidal fit ($p<0.05$) were considered to have a seasonal component. Adjusted R^2 was used as a measure for the fraction of variability explained by seasonality. The relative seasonal amplitude was interpreted as a measure for the relative importance of the seasonal cycle. The consistency of seasonal forcing was assessed by comparing the timing of the fitted seasonal maximum for a parameter between specimens. Results of seasonality analysis are found in **S12**.

Calcite-bound nitrogen isotope analysis

The nitrogen isotopic composition ($\delta^{15}N$) of organic matter bound to calcite in the foliated and chalky microstructures was measured following the protocols previously described for other fossil types (e.g. foraminifera, corals and otoliths; Ren et al 2009; Straub et al 2013; Wang et al 2014; 2016; Lueders-Dumont 2018). First, 7 ml of a solution of sodium dithionite ($Na_2S_2O_4$) and citric acid ($C_6H_8O_7$), adjusted to pH 8, was added to the samples, which were placed in an 80°C water bath for 30 minutes. After cooling, sample vials were centrifuged and the residues were rinsed three times with Milli-Q water and transferred to combusted 4 ml glass vials. Next, 3 ml of a basic potassium persulfate solution (recipe: 2 g sodium hydroxide, NaOH, + 2 g potassium persulfate, $K_2S_2O_8$ in 100 ml milliQ water) was added to the samples, and they were autoclaved for 60 minutes at 120°C. Samples were subsequently rinsed four times with milliQ water with a centrifugation step in between each rinse, and excess water was removed. Samples were then dried overnight at 60°C.

Dried sample powders were acidified with 45 microliters of 4N Optima Grade hydrochloric acid (HCl), and bivalve-bound organic N was oxidized to nitrate by reaction with 1 ml of basic potassium persulfate solution. The persulfate solution recipe is 0.67 g of 4-times recrystallized low-N $K_2S_2O_8$ and a spike of 4 mL of NaOH solution at 6.25mM, diluted up to 100 ml of milliQ water, and was prepared immediately before its addition to the samples, which were subsequently autoclaved for 1 hour at 120°C to ensure complete oxidation of the organic N. Amino acid isotope standards USGS40 and USGS41 ($\delta^{15}N$ values of -4.5‰ and +47.57 ‰ respectively) were oxidized concurrently with the samples to evaluate the reproducibility of the oxidation step of the procedure. Oxidation blanks were run to estimate the contribution and the isotopic composition of the blank of the oxidative step. On average, the fractional contribution of this oxidation blank to the N content of our samples was about 4%.

The pH of the samples was adjusted to 5-7 by small additions of 4N HCl. Nitrate concentration in the sample was measured by Vanadium(III) reduction and chemiluminescence with a NO_x analyzer to determine the appropriate volume of sample to aliquot for isotopic analysis. Isotopic composition and N content were measured using the 'denitrifier method', in which nitrate is quantitatively converted to nitrous oxide (N_2O) by denitrifying bacteria (Sigman et al., 2001; Weigand et al., 2016) . The N_2O was subsequently purified, concentrated, and analyzed for $\delta^{15}N$ using a purpose-built system coupled to a MAT 253 Plus gas-source stable isotope ratio mass spectrometer. Isotope values are reported relative to air through calibration with two nitrate isotopic references, IAEA-N3 and USGS-34 with known $\delta^{15}N$ values of 4.7‰ and -1.8‰, respectively. The precision of the entire procedure was 0.2‰ (1s) based on the measurement of our in-house coral standards.

Sulfur isotope analysis

Samples from the foliated and chalky microstructures of specimens **H2** and **H3** were weighed (~100-160 mg) into acid washed PFA vials (Savillex, Eden Prairie, MN, USA). Concentrated sub-boil distilled trace metal analysis grade HCl (Fisher Chemicals, Leicestershire, UK) was added in 20 µL steps to the sample with highest weight (~160 mg) until no visible reaction was observed and an additional 60 µL was added to be sure that the sample was fully reacted (in total 400 µL concentrated HCl was added). To all other samples 400 µL concentrated HCl was added directly and then all samples were evaporated to dryness on a 70°C hot plate. Residuals were re-dissolved in 2 mL 0.25% HCl (solution prepared with ultrapure Milli-Q water, resistivity ≥18.2 MΩcm) and an aliquot was sampled for concentration determination with triple quadrupole ICP-MS Agilent 8800 (Agilent Technologies, Santa Clara, USA). Sulfur in the samples was then purified twice with 2 mL strong cation exchange resin AG50-X8 (200-400 mesh, Bio-Rad) following the procedure in Paris et al. (2013). Purified solutions were collected into PFA vials and evaporated to dryness on a 70°C hot plate. Residuals were re-dissolved in 2 mL 0.3 mol/L sub-boil distilled trace metal analysis grade HNO_3 (Fisher Chemicals, Leicestershire, UK) awaiting sulfur ratio measurements. An aliquot was sampled for recovery (>95 %) and purity (sufficient removal of matrix elements after first purification step) estimation after each separation step with triple quadrupole ICP-MS. A procedural blank was treated in the same way as the samples throughout all steps.

Two internationally certified non-isotopic reference materials were treated as samples through the whole procedure and used to estimate expanded uncertainty of the sulfur isotope ratio values of the samples: powdered dolomite BAS ECRM782-1 (Bureau of Analysed Samples Ltd., Middlesbrough, UK) and powdered limestone NIST-1d (National Institute of Standards and Technology, Gaithersburg, MD, USA). These standards were digested, purified and measured at separate occasions (5 digestions for BAS ECRM782-1 and 6 digestions for NIST-1d), at two different laboratories. For accuracy determination a NIST915 certified calcium carbonate non-isotopic reference material was used both in pure form and spiked with 10 µg (~10 times lower S concentration than expected in the samples) in-house reference solution with calibrated $\delta^{34}S$ value (ICP-S: 1000 mg/L as $(NH_4)_2SO_4$ in water, $\delta^{34}S = 4.67 \pm 0.28$‰VCDT 2SD, n=75, Chem-Lab NV, Zedelgem, Belgium). The calibration of the ICP-S was performed throughout a year by bracketing with certified isotopic reference material IAEA S1 ($\delta^{34}S$ = -0.3‰ VCDT, International Atomic Energy Agency, Vienna, AT). The $\delta^{34}S$, expressed in delta notation with reference to the Vienna-Canyon Diablo Troilite (‰VCDT), values are calculated using a modified equation from Clough et al. (2006):

$$\delta^{34}S_{sample} = \left[\frac{(^{34}S/^{32}S)_{sample}}{(^{34}S/^{32}S)_{IAEA\text{-}S\text{-}1}} \times \left(\frac{(\delta^{34}S)_{IAEA\text{-}S\text{-}1}}{1000} + 1 \right) - 1 \right] \times 1000$$

Samples and standards were analyzed for their sulfur isotope composition ($\delta^{34}S$) using a Multiple Collector Inductively Coupled Plasma Mass Spectrometer (MC-ICP-MS; Neptune Plus, Thermo Fisher Scientific, Bremen, Germany). The MC-ICP-MS was equipped with jet sample cones for improved sensitivity and operated in high spectral resolution (HR) mode. The sample was introduced using a heated spray chamber coupled to a desolvating membrane (Aridus II, Teledyne Cetac, Omaha, NE, USA). Typical operating parameters are listed in **Table S2**.

All solutions were diluted to a sulfur concentration of 750 ng/mL in a 0.3 mol/L HNO_3 matrix and in accordance to Paris et al. (2013) sodium (10 000 mg/L, Chem-Lab NV Zedelgem, Belgium) was added to a concentration of 1275 ng/mL to increase the sulfur sensitivity by improving transport efficiency of sulfur through the membrane in the desolvating membrane. Additionally 4000 ng/mL silicon (1000 mg/L, Chem-Lab NV Zedelgem, Belgium) was added to all solutions to correct for matrix effects and signal fluctuations during the measurement, using the ratio $^{29}Si/^{30}Si$ as a proxy for the S isotope ratios, since both elements are assumed to behave similarly in the ICP plasma (Giner Martínez-Sierra et al., 2010). The Si internal standard correction was performed using the Baxter approach, a revised version of the Russel law (Baxter et al., 2006). Samples and standards were diluted separately and measured several times on different days to obtain a more reliable $\delta^{34}S$ value (10-14 measurements/sample). The solutions were bracketed by IAEA S1 using the bracket-sample-bracket approach the first measurement day and by ICP-S the rest of the measurement days, to correct for mass bias drift. Between each measurement solution, a 0.3 mol/L HNO_3 wash solution was aspirated until the signal reached background levels (~2 min). Blank subtraction of the S isotope intensities of the diluted blank from the S isotope intensities of the sample, for the samples the procedural blank was used (<1.5% of the sample signals) and for the spiked NIST915 standard the unspiked NIST915 was used (<17% of the sample signals). The corresponding blanks were measured close to the corresponding sample, to minimize influence of drift.

As the sample amounts were limited, multiple separate digestions for each sample were not possible to estimate uncertainty of the whole procedure. NIST-1d and BAS ECRM783-1 were used as a proxy to the samples as they have a similar matrix as the sample. Expanded uncertainty for the samples was calculated using the mean standard deviation from the NIST-1d (SD=0.36‰, n=6) and BAS ECRM783-1 (SD=0.15‰, n=5) measurements, with a coverage factor k=2 (2σ).

The $\delta^{34}S$ value for the spiked NIST915 standard (4.80 $\pm$ 0.22‰VCDT 2SD, 8 measurements with 3 dilutions over 3 days) corresponded well with the calibrated expected value for the in-house standard ICP-S. The method applied to carbonate samples was therefore deemed accurate, even for S concentrations much lower than for the samples and for higher blank levels.

Table S2. Typical MC-ICP-MS and desolvator operating parameters for S isotope ratio measurements.

MC-ICP-MS	
MC-ICP-MS	Neptune Plus (Thermo Fisher Scientific)
RF power	1200 W
Sample cone	Jet (Ni)
Interface cone	X-skimmer (Ni)
Resolution	High
Auxiliary gas	0.8 L min^{-1}
Sample gas	0.8-0.9 L min^{-1}
Cup configuration	L4 (^{29}Si), L2 (^{30}Si), H1(^{32}S), H2(^{33}S), H4 (^{34}S)
Data acquisition	4.192 s integration, 1 block, 45 cycles
Desolvator	
Desolvator	Aridus II
Nebulizer	PFA 100 (ESI)

Sweep gas	11-13 L min^{-1}
Nitrogen gas	0 L min^{-1}
Flow rate	100 µg min^{-1}
Spray chamber (PFA) temperature	110 °C
Desolvator temperature	160 °C

Supplementary result figures and tables

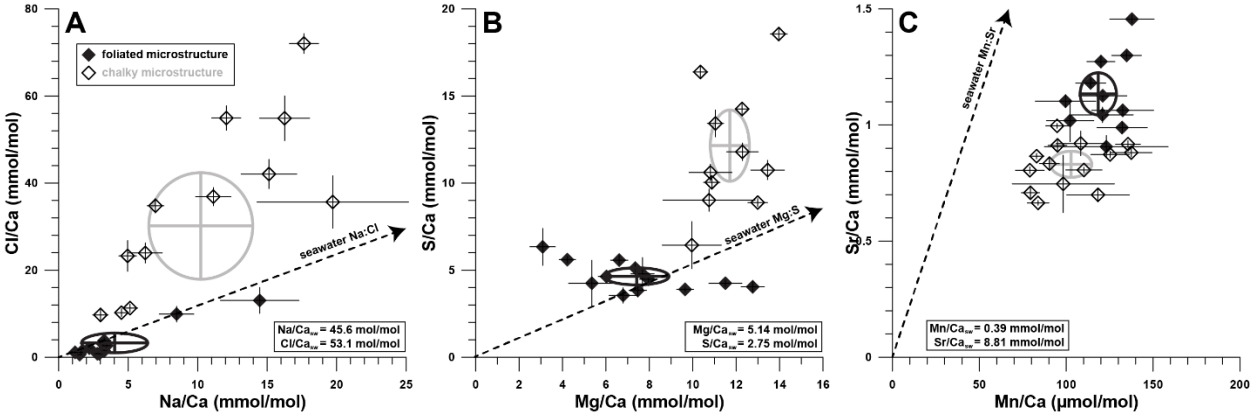

Figure S2: *Cross plots of molar concentration ratios of (**A**) Na/Ca vs. Cl/Ca, (**B**) Mg/Ca vs. S/Ca and (**C**) Mn/Ca vs. Sr/Ca. Open symbols indicate averages of measurements in the chalky microstructure for specimens, while closed symbols represent foliated microstructure concentrations. Horizontal and vertical lines crossing inside symbols show uncertainty (95% confidence level) within specimens. Grey and black ellipses represent inter-specimen uncertainty of chalky and foliated microstructures, respectively, and are centered on microstructural averages. Dashed arrows indicate the trace element ratio in seawater and the direction of seawater trace element to Ca ratios. Values in rectangular boxes indicate the actual seawater trace element ratios for comparison (after Pilson, 2012 and van Hulten et al. 2016; see also **Fig. 5** in main text).*

Table S3 *Overview of age model results showing the R^2 of modelled versus measured Mg/Ca, modelled ages of the specimens in days and years and average growth rates for the microstructures. Uncertainties are given as 95% confidence levels.*

Locality	Specimen	R2 (sampled vs modelled Mg/Ca)	Specimen age (days)	Specimen age (years)	growth rate (µm/d) foliated microstructure	GR (µm/d) chalky microstructure
BR	O1	0.45	946	2.59	34.6 ±1.5	52.2 ±5.3
	O2	0.80	849	2.33	21.4 ±0.7	19.7 ±1.5
	O3	0.68	887	2.43	22.1 ±1.5	50.0 ±2.4
	O4	0.61	601	1.65	75.2 ±2.4	54.3 ±2.4
	O5	0.12	624	1.71	23.1 ±1.0	29.7 ±4.4
	O6	0.55	1072	2.94	18.8 ±1.0	16.3 ±1.0
	O7	0.41	1526	4.18	31.3 ±1.5	27.7 ±2.8
	O8	0.85	723	1.98	40.5 ±2.7	61.1 ±4.3
TH & MB	H4	0.49	756	2.07	71.0 ±5.5	86.3 ±4.1
	M4	0.78	1890	5.18	16.0 ±1.1	25.6 ±3.5
	M5	0.94	1958	5.37	25.3 ±1.4	37.0 ±4.4
	M6	0.91	1524	4.18	16.7 ±1.0	44.4 ±4.7
Combined	average	0.63	1113	3.05	33.0 ±4.2	42.0 ±5.2

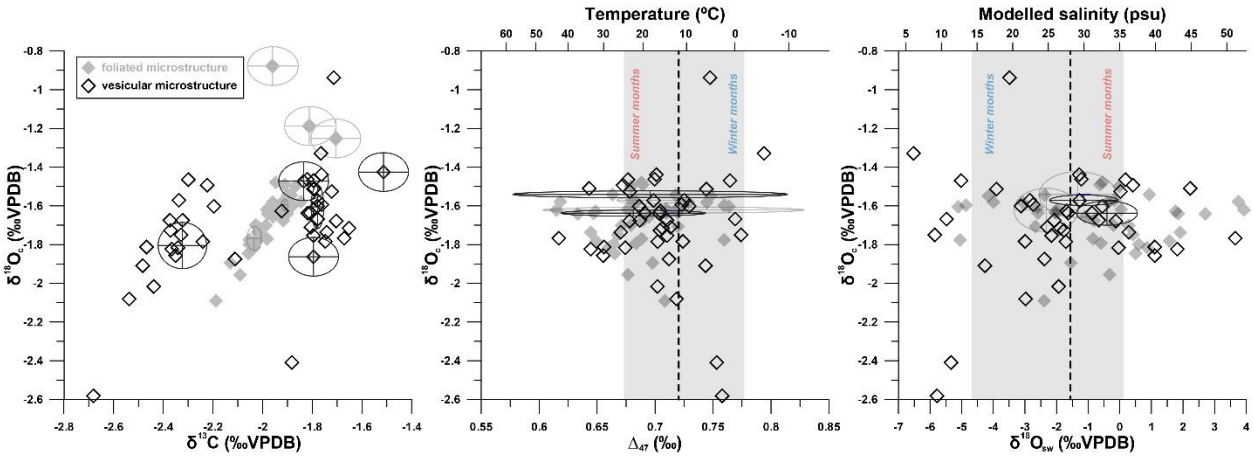

Figure S3*: Cross plots of carbonate stable isotope results, with (**A**) $\delta^{18}O$ plotted against $\delta^{13}C$, (**B**) $\delta^{18}O$ plotted against Δ_{47} and reconstructed calcification temperature and (**C**) $\delta^{18}O$ plotted against the reconstructed $\delta^{18}O$ composition of the sea water ($\delta^{18}O_{sw}$). Grey and black ellipses represent inter-specimen uncertainty of chalky and foliated microstructures, respectively, and are centered on microstructural averages. Grey bars and dashed vertical lines in **B** and **C** indicate* in situ *measured seasonal ranges and mean annual averages in sea surface temperature (**B**) and sea surface salinity (**C**), respectively. Sea surface salinity values corresponding to $\delta^{18}O_{sw}$ reconstructions were calculated by inverting the mass balance model outlined in **2.7** of the main text (see also explanation above).*

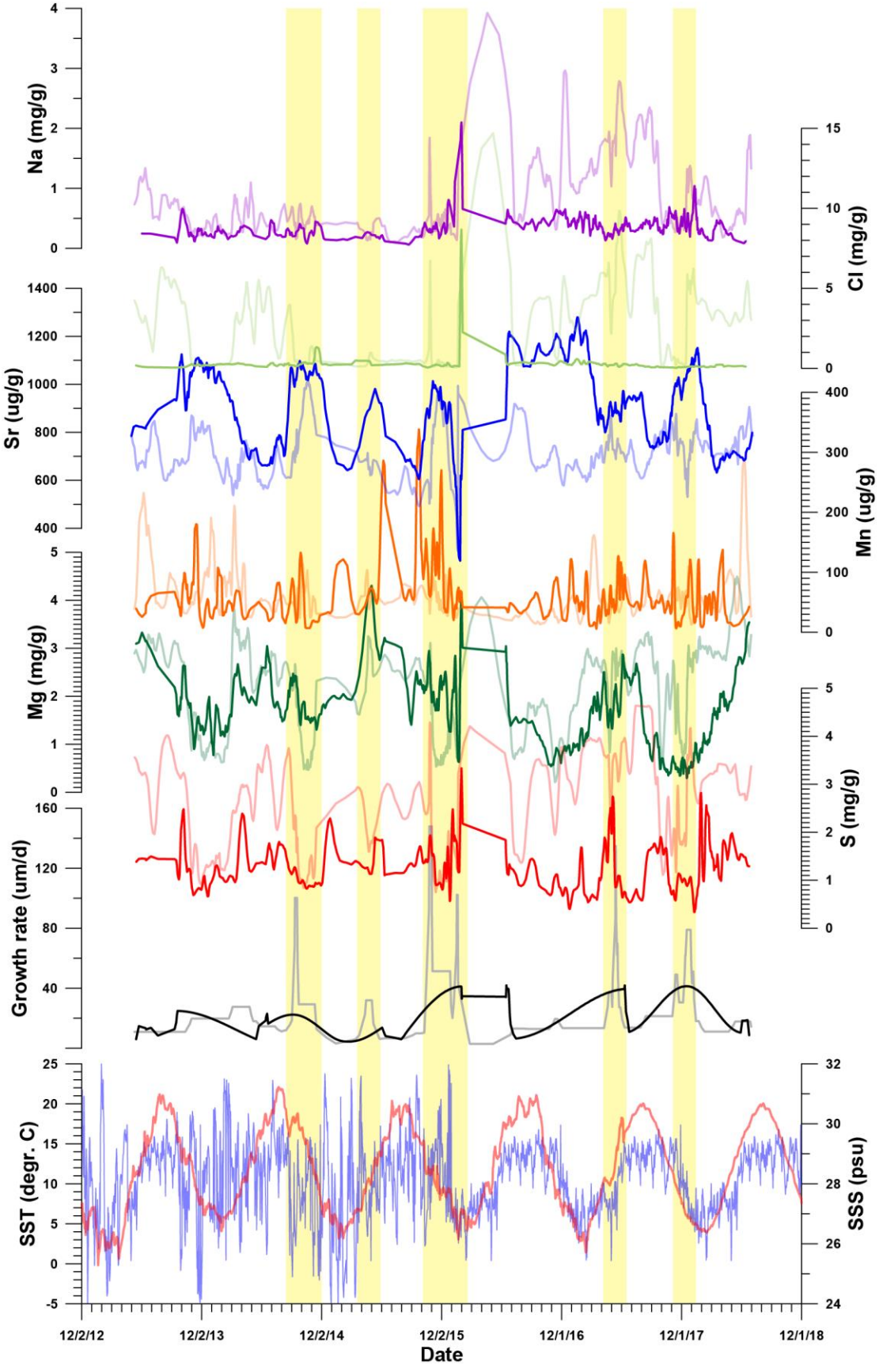
Na (mg/g)
Cl (mg/g)
Sr (ug/g)
Mn (ug/g)
Mg (mg/g)
S (mg/g)
Growth rate (um/d)
SST (degr. C)
SSS (psu)
12/2/12
12/2/13
12/2/14
12/2/15
12/1/16
12/1/17
12/1/18
Date

***Figure S4**: Trace element (Na, Mg, S, Cl, Mn and Sr) profiles measured using µXRF plotted together with age model results (growth rate in measurement direction) and environmental conditions (sea surface temperature in red and sea surface salinity in blue) on a common time axis. In trace element and growth rate plots, transparent lines indicate profiles through both microstructures (including the chalky structure) while solid lines indicate profiles exclusively through the foliated calcite. Vertical yellow bands indicate the positions where the line through mixed microstructures (transparent lines) samples the chalky microstructure. Note how growth rates increase sharply in these parts of the measurement, but only in the profile through both measurements, indicating higher growth rate of the chalky microstructure compared to the foliated structure forming at the same time under the same conditions. Note also that these chalky lenses, in this specimen, are almost exclusively formed in the spring or autumn season. This may explain the comparatively closer match between temperatures reconstructed from the chalky microstructure than from the foliated microstructure (see main text).*

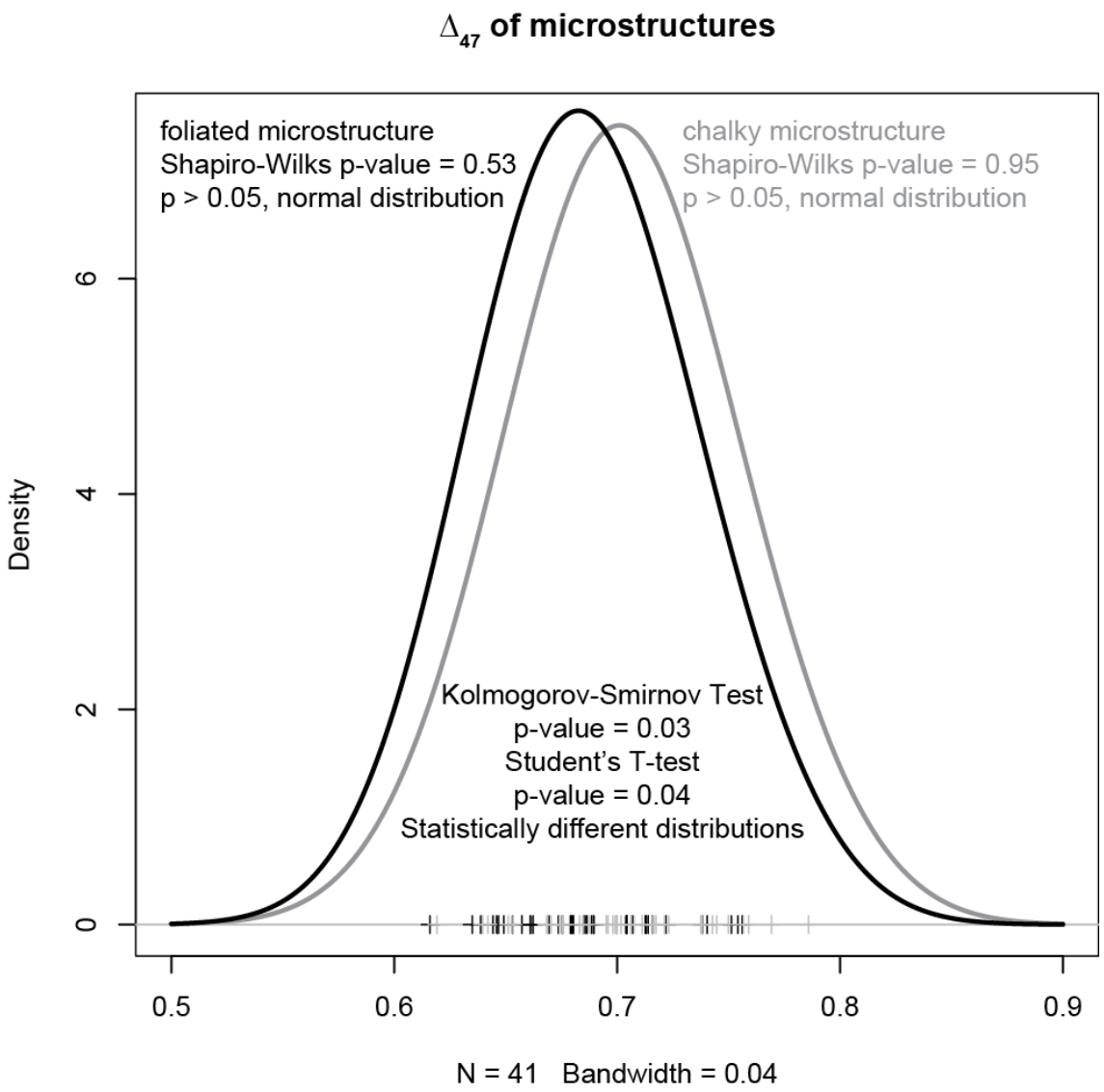

***Figure S5**: Shows the kernel-smoothed normal distribution of clumped isotope (Δ_{47}) measurements in the chalky (grey) and foliated (black) microstructures. The values of individual measurements in the distributions are indicated as crosses on the horizontal line at zero density. Statistical tests (Kolmogorov-Smirnov test p = 0.03; Student's t-test p = 0.04) show that these samples were likely (95% confidence level)*

*sampled from different distributions with statistically significant difference between their means, indicating a statistically significant difference between the microstructures at the 95% confidence level. A script detailing the calculations for this plot is provided in **S14**.*

References

Baxter D.C., Rodushkin I., Engström E. and Malinovsky D. (2006) Revised exponential model for mass bias correction using an internal standard for isotope abundance ratio measurements by multi-collector inductively coupled plasma mass spectrometry. *Journal of Analytical Atomic Spectrometry* **21**, 427–430.

Clough R., Evans P., Catterick T. and Evans E. H. (2006) $\delta^{34}S$ Measurements of Sulfur by Multicollector Inductively Coupled Plasma Mass Spectrometry. *Anal. Chem.* **78**, 6126-6132.

de Winter N. J. and Claeys P. (2016) Micro X-ray fluorescence (μXRF) line scanning on Cretaceous rudist bivalves: A new method for reproducible trace element profiles in bivalve calcite ed. M. R. Petrizzo. Sedimentology **64**, 231–251.

de Winter N. J., Goderis S., Dehairs F., Jagt J. W., Fraaije R. H., Van Malderen S. J., Vanhaecke F. and Claeys P. (2017) Tropical seasonality in the late Campanian (late Cretaceous): Comparison between multiproxy records from three bivalve taxa from Oman. Palaeogeography, Palaeoclimatology, Palaeoecology **485**, 740–760.

Giner Martínez-Sierra J., Santamaria-Fernandez R., Hearn R., Marchante Gayón J.M. and García Alonso J.I. (2010) Development of a direct procedure for the measurement of sulfur isotope variability in beers by MC-ICP-MS. *J Agric Food Chem.* **58** (7), 4043-4050.

Harwood A. J. P., Dennis P. F., Marca A. D., Pilling G. M. and Millner R. S. (2008) The oxygen isotope composition of water masses within the North Sea. *Estuarine, Coastal and Shelf Science* **78**, 353–359.

Judd E. J., Wilkinson B. H. and Ivany L. C. (2018) The life and time of clams: Derivation of intra-annual growth rates from high-resolution oxygen isotope profiles. Palaeogeography, Palaeoclimatology, Palaeoecology **490**, 70–83.

Mook W. G. (1970) Stable carbon and oxygen isotopes of natural waters in the Netherlands. *Isotope hydrology* **1970**, 163–190.

Paris G., Sessions A. L., Subhas A. V. and Adkins J. F. (2013) MC-ICP-MS measurement of δ34S and ∆33S in small amounts of dissolved sulfate. *Chemical Geology* **345**, 50–61.

Pilson M. E. (2012) *An Introduction to the Chemistry of the Sea*., cambridge university press.

Quinby-Hunt M. S. and Turehian K. K. (1983) Distribution of elements in sea water. *Eos, Transactions American Geophysical Union* **64**, 130–130.

Sigman D. M., Casciotti K. L., Andreani M., Barford C., Galanter M. and Böhlke J. K. (2001) A bacterial method for the nitrogen isotopic analysis of nitrate in seawater and freshwater. *Analytical chemistry* **73**, 4145–4153.

van Hulten M. M. P., Middag R., Dutay J.-C., de Baar H. J. W., Roy-Barman M., Gehlen M., Tagliabue A. and Sterl A. (2016) Manganese in the West Atlantic Ocean in context of the first global ocean circulation model of manganese. *arXiv preprint arXiv:1606.07128*.

Vansteenberge S., de Winter N. J., Sinnesael M., Xueqin Z., Verheyden S. and Claeys P. (2020) Benchtop μXRF as a tool for speleothem trace elemental analysis: Validation, limitations and application on an Eemian to early Weichselian (125–97 ka) stalagmite from Belgium. Palaeogeography, Palaeoclimatology, Palaeoecology **538**, 109460.

Witbaard R., Jenness M. I., Van Der Borg K. and Ganssen G. (1994) Verification of annual growth increments in Arctica islandica L. from the North Sea by means of oxygen and carbon isotopes. *Netherlands Journal of Sea Research* **33**, 91–101.